Aerodynamic Validation of Wind Turbine Airfoil Models in the Virginia Tech Stability Wind Tunnel

NAWEA 2015 - Blacksburg, VA - June 9–11, 2015

Matthew S. Kuester, Ken Brown, Timothy Meyers, Nanyaporn Intaratep, Aurélien Borgoltz, and William J. Devenport

Department of Aerospace and Ocean Engineering, Virginia Polytechnic Institute and State University, Blacksburg, VA

1 Introduction

Accurate predictions of lift and drag are critical for the design and performance evaluation of megawatt-scale wind turbines. Wind tunnel testing is a key component of the design process, as it complements CFD and other prediction tools. Over the last 10 years, the Virginia Tech Stability Wind Tunnel has been used extensively for aerodynamic and aeroacoustic measurements of wind turbine airfoils; however, comparisons of data from Virginia Tech and other wind tunnels showed discrepancies in lift curve slope and maximum lift coefficient. For a DU96-W-180 airfoil geometry, measurements at Virginia Tech yielded lift curve slopes 3.0% – 5.5% smaller and maximum lift coefficients 0.04–0.12 smaller than measurements from two large scale European wind tunnels. Although differences in lift curve slopes and maximum lift coefficients are not uncommon in wind tunnel testing (see McCroskey [1] and Troldborg *et al.* [2]), this was viewed as an opportunity to thoroughly investigate airfoil testing procedures.

The goal of this work is to investigate and evaluate all aspects of airfoil model testing in the Virginia Tech Stability Tunnel, from model fabrication through data reduction. This work has validated the majority of aspects/procedures of the Virginia Tech Stability Tunnel, including the accuracy of measured reference conditions, tunnel flow quality, accuracy of model outer mold line, lift & drag repeatability, and end effects on maximum lift. The results presented in the rest of the paper highlight key findings warranting further study.

2 Wind Tunnel Facility

These experiments were performed in the Virginia Tech Stability Wind Tunnel. A thorough description of the tunnel is given by Devenport *et al.* [3], while a brief description is given here. The wind tunnel is a closed return, low-turbulence tunnel capable of reaching freestream speeds up to 75 m/s. The test section is 24 ft. long with a 6 ft. $\times$ 6 ft. square cross section. Turbulence levels in the test section are less than 0.03%. Two different test sections provide different capabilities: an anechoic test section with Kevlar windows is used for aeroacoustic testing, and an aerodynamic test section with aluminum walls is used for extensive aerodynamic measurements. Airfoil models are mounted vertically along the centerline of the test section. Lift is measured through airfoil pressure taps and wall pressure taps (in the aerodynamic test section), while drag is measured using a traversing Pitot-static wake rake that horizontally spans the entire test section.

A 0.8 m chord DU96-W-180 model was mounted in the aerodynamic test section for this work. This model was constructed at Virginia Tech by the Aerospace and Ocean Engineering Machine Shop. The model is constructed of CNC-machined aluminum laminates. The 50-mm thick laminates are stacked in the span direction, pinned together, and held in compression. The model is rotated to the desired angle of attack through a turntable mounted in the ceiling, and the angle of attack is measured using an encoder

Figure 1: Naphthalene visualization on pressure side of the DU96-W-180 model at $\alpha = 8°$ and $\mathrm{Re_c} = 3.0$ Million. Left: after naphthalene application. Right: after wind tunnel was held on condition for ∼10 minutes and turned off.

on the turntable. A suction system is used to remove the wall boundary layer on both the floor and ceiling to minimize end effects. The gap between the model tips and wind tunnel floor/ceiling is nominally five millimeters wide to allow an adequate flow rate through the suction system. Brown *et al.* [4] provide more details regarding the mounting and testing of airfoil models in the Virginia Tech Stability Wind Tunnel.

Unless otherwise noted, all measurements were performed at a chord Reynolds number ($\mathrm{Re_c}$) of 3.0 Million, which corresponds to approximately 60 m/s (depending on the temperature and atmospheric conditions.)

3 Surface Quality & Boundary Layer Transition

One of the objectives of this work was to determine if model surface quality was tripping the boundary layer and thus affecting lift measurements. The Stability Tunnel utilizes infrared thermography to visualize boundary layer transition on airfoil models; however, this measurement is typically made with a thin insulative material on the airfoil surface. For this work, naphthalene visualization was used to highlight transition on the clean DU96-W-180 model without any surface treatments.

Figure 1 shows an example of the before and after photographs from a naphthalene visualization. In this technique, naphthalene is dissolved in acetone and pressure sprayed onto the model. The pressure on the sprayer is adjusted so the acetone evaporates within 1–2 seconds, leaving a thin coat of naphthalene on the model. The tunnel is then set to the test condition, and the model is rotated to the desired angle of attack. The naphthalene sublimates at a rate proportional to shear stress, so the naphthalene disappears rapidly from the model where the boundary layer is turbulent. The flow is turned off once a clear transition front is observed (typically around 5-10 minutes).

Naphthalene visualization was performed at several angles of attack between -8 and 11 degrees at $\mathrm{Re_c} = 3.0$ Million. The naphthalene showed that small surface defects at the edges of laminates caused turbulent wedges. In addition, forty-micron-thick tape, which was covering threaded holes on the pressure side of the model, was also tripping the boundary layer and creating turbulent wedges. Figure 2 shows examples of tape and laminate edges tripping the boundary layer on both the pressure and suction sides of the model.

After each naphthalene visualization, surface defects that caused turbulent wedges were lightly sanded

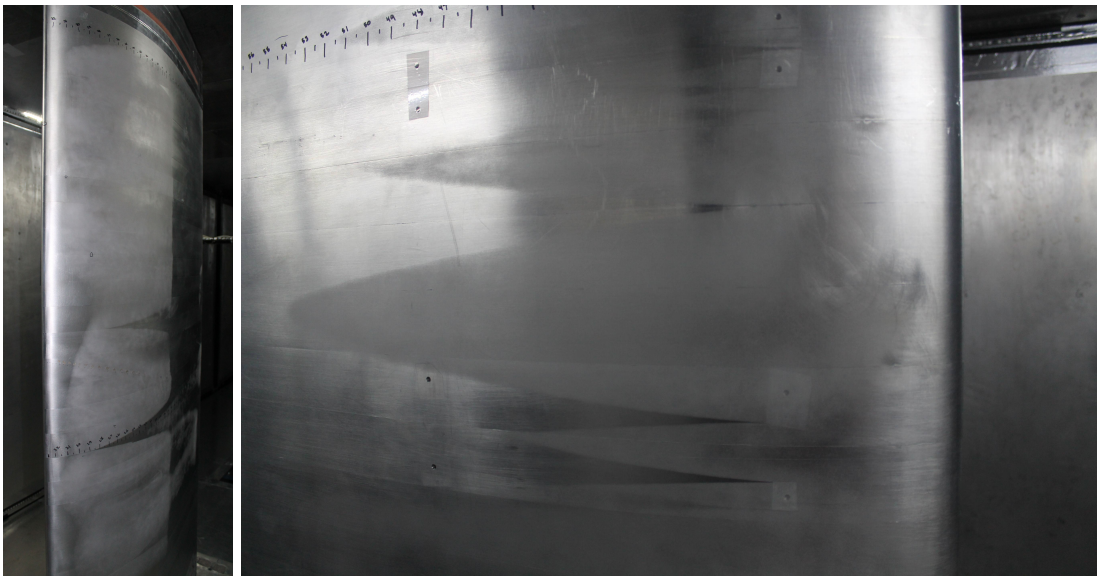

Figure 2: Naphthalene visualization on the DU96-W-180 model at $Re_c = 3.0$ Million. Left: suction side at $\alpha = 0$ degrees, flow from left to right. Right: pressure side at $\alpha = 8$ degrees, flow from right to left. Turbulent wedges caused by forty-micron-thick tape and surface defects at laminate edges.

and polished until as many turbulent wedges were removed as possible. All forty-micron tape was removed from the model, and the threaded holes were filled with autobody filler and sanded flush with the surface. Figure 3 shows the effect of improving the surface quality on lift. Improving the model surface finish increased the measured lift curve slope (between 0 & 5 degrees) over 3% and slightly raised the maximum lift coefficient.

The number of turbulent wedges caused by defects on laminate edges may be unique to the DU96-W-180 model. This particular model has been used for multiple research studies, and as such it has been disassembled and reassembled multiple times. Each time the model is modified, the edges of the laminates are exposed to additional wear. Over time, this additional wear led to the large number of turbulent wedges caused by surface defects. New models, which have only been assembled once, would not have this issue; nevertheless, naphthalene visualization is now a standard procedure for tests on airfoil models to ensure model surface finish is not prematurely causing boundary layer transition.

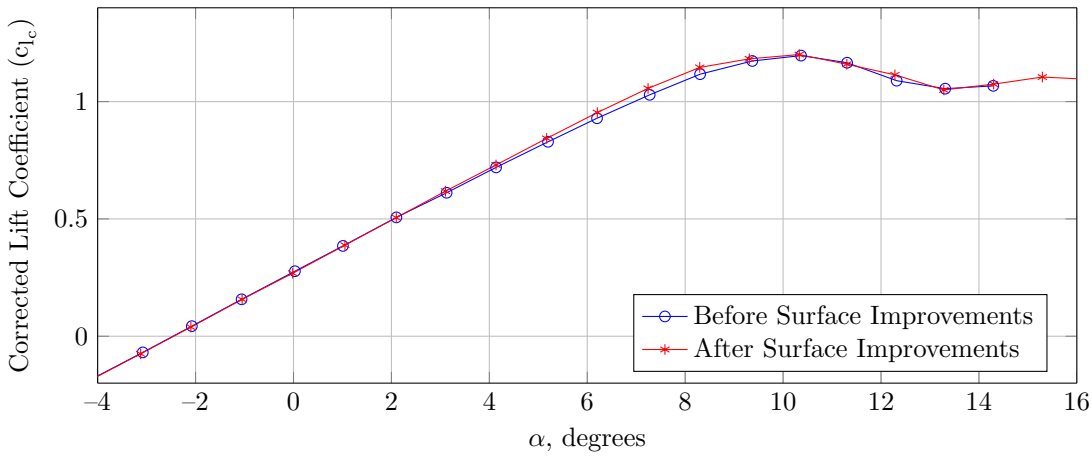

Figure 3: Lift curve improvements at $Re_c = 3.0$ Million after improving the surface quality.

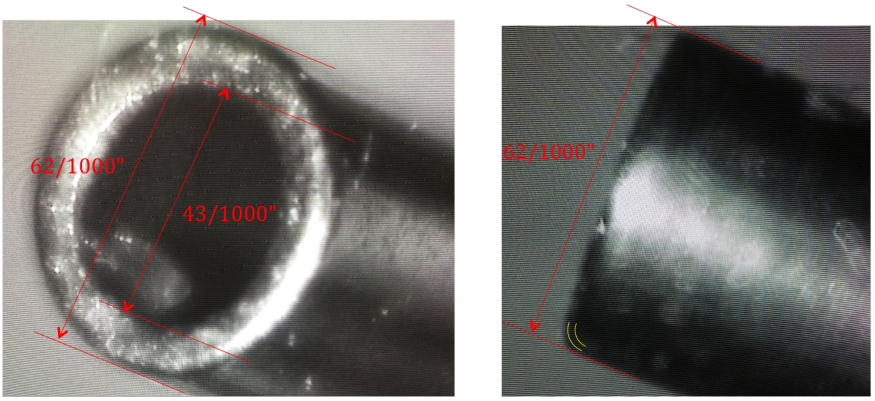

Figure 4: Microscope views of a 1.0 mm ID tube used for a pressure tap.

Table 1: Descriptions and locations of added pressure taps.

Tap	Side	z/span	x/c	Tap Description
P1	Pressure	0.369	0.200	1.0 mm ID tube, rounded edge
P2	Pressure	0.353	0.200	1.0 mm ID tube, clean edge
P3	Pressure	0.361	0.200	0.5 mm ID tube, clean edge
S1	Suction	0.361	0.050	1.0 mm drilled
S2	Suction	0.369	0.050	0.5 mm drilled
S3	Suction	0.353	0.050	0.3 mm drilled

4 Pressure Taps

Another item that was investigated during validation testing was the effect of pressure tap size and construction. The DU96-W-180 model has 79 pressure taps near mid-span (one port at the leading edge and 39 ports on both the suction and pressure sides.) The taps are staggered in the span direction to avoid interference effects. Taps at the leading and trailing edges were drilled using a 0.04" bit and deburred/cleaned, while taps along the mid-chord (12.6% to 74.6% chord) were installed by inserting a small diameter tube flush with the airfoil surface. The 'tube' taps were implemented to decrease manufacturing time and costs.

Figure 4 shows the end of a tube used for installing pressure taps. The end of the tube has a 0.0004" radius on the outer edge, which creates a groove around the pressure tap when the end is installed flush with the airfoil surface. The majority of the tube pressure taps do not have this groove because the tube had to be cut before installation. To avoid this issue with future models, all newly installed tubed pressure taps will have a cut end to avoid this groove.

The effect of pressure tap diameters/geometries was examined by adding six additional pressure taps to a single DU96-W-180 laminate. Information about the added taps is shown in Table 1. Three of the taps were installed on the pressure side at 20% chord, while the remaining three taps were installed on the suction side at 5% chord. The added taps were installed near 1/3 span and were separated by 0.8" in the spanwise direction. These taps were chosen to specifically study the effects of pressure tap diameter and the effect of the 0.004" groove surrounding some of the tube pressure taps.

Figure 5 shows the pressure coefficients measured by the added taps as a function of angle of attack. In the linear region of the lift-curve slope, the differences between the three taps on each side of the airfoil are within the uncertainty of the pressure measurement. Once the airfoil has stalled (past $\alpha = 10^\circ$ on the suction side), the spread between the measurements becomes much larger. This spread is caused by spanwise variations in the pressure field caused by trailing-edge separation at stall and was not repeatable.

Interestingly, the spread in the measurements increases when the taps are in a turbulent boundary layer compared to a laminar boundary layer. Infrared thermography measurements identified transition locations on both sides of the model as a function of angle of attack. The transition line crosses x/c = 20% on the pressure side between –4° and –5° angle of attack, and the transition line crosses x/c = 5% on the suction

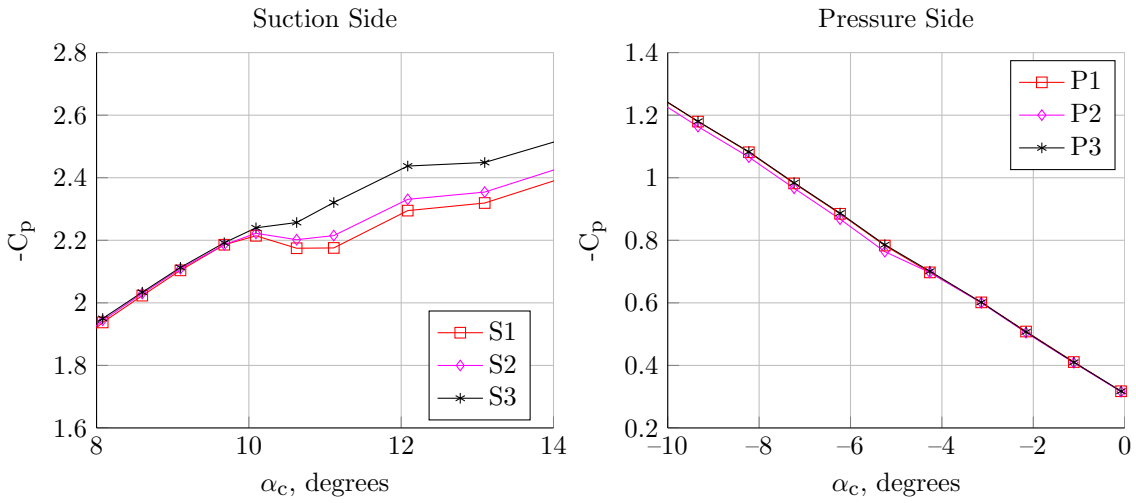

Figure 5: Pressure coefficients measured by the six additional pressure taps.

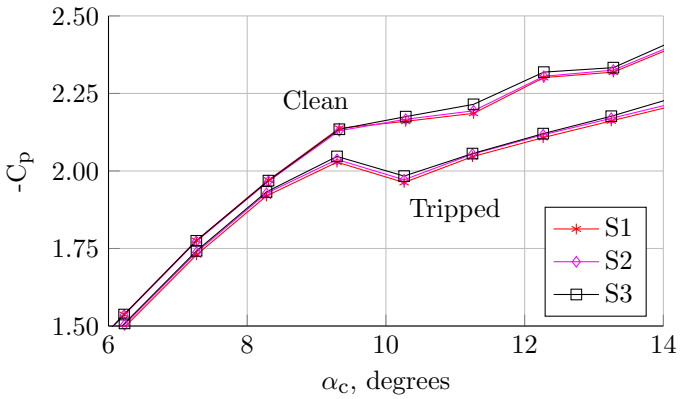

Figure 6: Effect of tripping on measured pressure coefficients from the three additional taps on the suction side of the airfoil.

side between 9° and 10° angle of attack. These angles correspond to an increased spread in the pressure measurements on both sides of the airfoil. On the pressure side, the spread in the measurements does not show a clear ordering according to tap geometry. The 0.5 mm tube with the cut end and the 1.0 mm tube with the non-cut end measured similar pressures in the turbulent boundary layer, but the 1.0 mm tube with the cut end measured a slightly higher pressure. On the suction side, the spread in the measurements correlates to the size of the tap; the smallest tap measured the lowest pressure, while the largest tap measured the largest pressure.

To confirm the differences in the pressure measurements between taps only occur in turbulent boundary layers, the three taps on the suction side were tripped at 2% chord in a subsequent test. Figure 6 compares the suction side tap measurements, before and after the trip was applied. In the clean case, the pressure measurements are self-consistent below 10°, where the boundary layer is laminar. In contrast, the tripped cases shows a spread in the measurement that persists both below and above 10°. This confirms the pressure bias of the different taps in turbulent boundary layers.

The tap diameter effects observed on the suction side can be explained by the work of Shaw [5], who extensively studied static pressure measurement biases in turbulent pipe flows. His work showed that there is a bias error with static pressure taps in turbulent flows. This bias, Δp, is proportional to $\tau_w \Pi(d^+)$. The function $\Pi(d^+)$, shown in Fig. 7(a), was determined experimentally and reaches this form of the curve for large values of length to diameter ratio. To confirm the applicability of Shaw's correction to the current experiment,

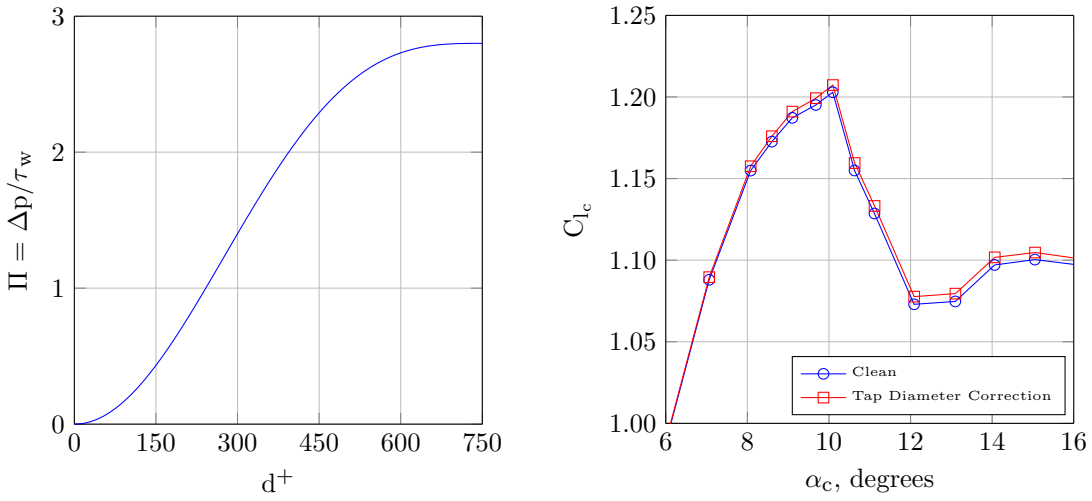

(a) Static pressure tap error function, from Shaw [5]

(b) Effect of tap correction on lift.

Figure 7: Pressure tap corrections for the DU96-W-180 at $Re_c = 3.0$ Million.

the correction was applied to the tripped data shown in Fig. 6 at $\alpha = 10.2°$. Skin friction was estimated using the boundary layer solver built into XFOIL, which was run at conditions that matched the experiment. The difference in pressure coefficient between the 0.3 mm and 1.0 mm diameter tap pressures in the experiment was 0.021, while Shaw's correction predicts that the difference between the two pressure coefficients should be 0.013. Despite the uncertainty in calculating shear stress using XFOIL, Shaw's correction predicted a pressure difference that is the same order of magnitude as the experiment.

Shaw's correction was further applied to the main pressure taps on the airfoil to estimate how much this effect may bias lift measurements. For each experimental measurement, XFOIL was run at the matching Reynolds number and angle of attack. The skin friction estimates from XFOIL were used to calculate d^+ for each pressure tap and apply the ΔC_p correction. Pressure taps that were upstream of natural transition were not corrected. The results from this analysis for a clean lift polar are shown in Fig. 7(b). Predicted values of d^+ were less than 300, with typical values less than 50. The changes in lift coefficient were only noticeable near positive stall (0.004 difference).

The effects of pressure tap diameter on airfoil lift measurements appear small, but should not be ignored when making high fidelity measurements. The preceding calculations have motivated a reduced (0.5 mm ID) standard tap size on all new models manufactured at Virginia Tech in order to reduce this pressure bias in turbulent boundary layers.

Another pressure tap related challenge encountered during testing was a turbulent wedge created by one of the leading edge pressure ports. The wedge appears on the suction side for positive angles of attack. Figure 8 shows naphthalene images of the turbulent wedge at $\alpha = 8°$ and $\alpha = 11°$. At 8°, the edge of the turbulent wedge runs next to the downstream pressure taps. In contrast, at 11°, the half-spreading angle of the turbulent wedge is larger than tap stagger angle (16.7°), and the wedge envelops the downstream taps.

Since turbulent wedges can affect airfoil pressure measurements, tap-induced wedges should be avoided. Lightly sanding around the 1.0 mm leading edge ports did not remove the turbulent wedge. The 1.0 mm hole size, along with the strong pressure gradient created by the suction peak at positive angles of attack, is the likely cause for this turbulent wedge. Naphthalene tests on other models, which have 0.5 mm ID taps, did not show a turbulent wedge created by pressure taps. This suggests that using 0.5 mm diameter taps will reduce the possibility of tap tripping at the leading edge.

5 Corrections for Model Deflection

Another focus of the validation testing was assessing deflection/flexure of the model and its mounting system under aerodynamic loading. As a first step towards this goal, laser distance sensors were installed into the

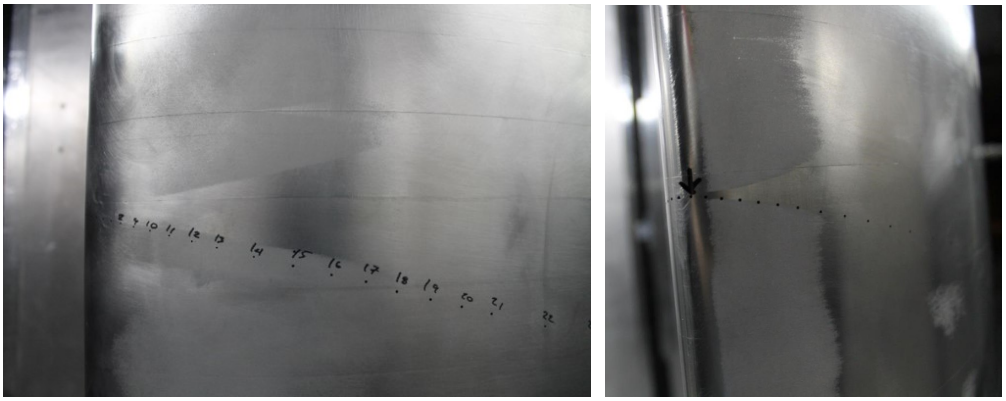

(a) $\alpha = 8^\circ$ (b) $\alpha = 11^\circ$

Figure 8: Turbulent wedge created by leading-edge pressure port at $Re_c = 3.0$ Million.

walls of the aerodynamic test section. This was done in two phases: in the first phase, a single laser was installed in the starboard wall of the test section. The laser hit the model near 1/3 span, approximately 8 inches below the pressure taps and 15 inches downstream of the center of rotation. This sensor continuously measured the distance between the wall and the airfoil model, and the model angle of attack was inferred from the model profile and the laser position/orientation. Figure 9 shows the orientation of the laser and the model within the test section.

A one time calibration was used to determine the laser's position and orientation relative to the model center of rotation. With the wind turned off, the model was rotated between –20° and 20° angle of attack in 1° increments. The angle of attack and measured laser distance at each point was used by an optimization routine to calculate the position and orientation of the laser relative to the model center of rotation. This calibration was then used to determine the angle of attack of the model, given the distance measurement from the laser. This conversion from laser distance to model angle of attack assumes that the center of rotation of the model does not shift. The residuals from the calibration data showed that the laser could measure the unloaded model angle of attack to within ± 0.02 degrees.

For the initial test of the laser system, the model was held at constant encoder angles of attack while the freestream speed was increased. Figure 10 shows the model deflection for $\alpha_{encoder} = 6^\circ$ and –11°, which correspond to $c_l \sim \pm 0.95$. Below 30 m/s, the model rotation was less than the uncertainty of the laser system. As the speed was further increased, the model rotated in such a way as to decrease the force on the model. For $\alpha_{encoder} = 6^\circ$, the laser indicated that model was rotating to a smaller angle of attack, while the opposite occurred at $\alpha_{encoder} = -11^\circ$.

Figure 11 compares $\alpha_{encoder}$ and α_{laser} for two angle sweeps at $Re_c = 3.0$ Million. The difference between the encoder and the laser shows a repeatable rotation of the model under aerodynamic loading. A large change in the moment coefficient across negative stall creates a sudden change in laser angle of attack. In the linear range of the lift curve, the difference between the encoder and the laser angles steadily decreases. At and beyond positive stall, the difference remains constant at -0.35 degrees. The lift curve slope (calculated between zero & five degrees) based on the laser is 1.6% larger than than the lift curve slope based on the encoder, indicating model deflection is partially responsible for discrepancies in lift curve slope between the Stability Tunnel and other facilities.

Based on these initial measurements, three additional sensors were installed in the wind tunnel walls. Figure 12 shows the layout of the phase 2 laser system. Two of the additional sensors were installed in the port wall; one of the lasers was installed 6 inches upstream of the center of rotation, while the second laser hit the model approximately 15 inches downstream of the center of rotation. The two lasers in the port wall were installed at the same span location in order to measure displacement of the model independent of rotation. The original laser, now defined as laser #3, was re-installed upside down to measure the model 8 inches off of the floor. The final laser was installed 11 inches below the ceiling.

The additional laser measurements clearly showed both translation and rotation of the model under aerodynamic loads. Figure 13 shows the difference between the measured laser angles and the encoder angle

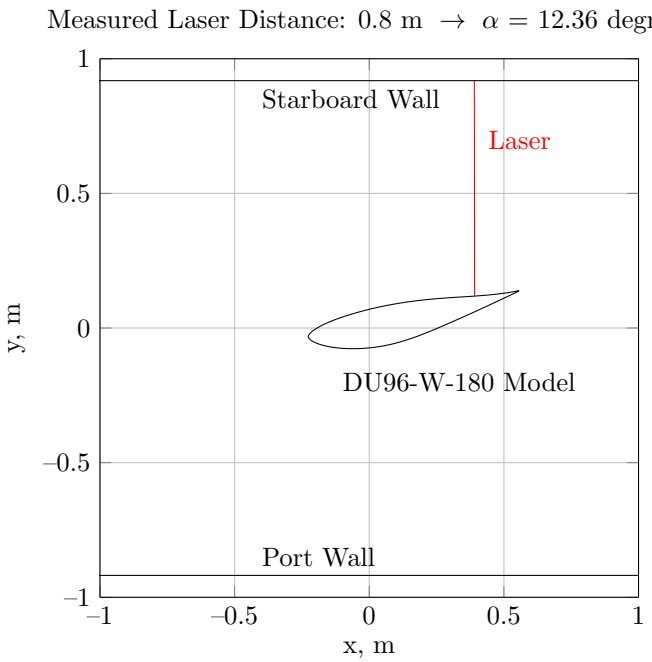

Figure 9: Top view of the laser setup of the laser distance sensor. Flow travels from left to right.

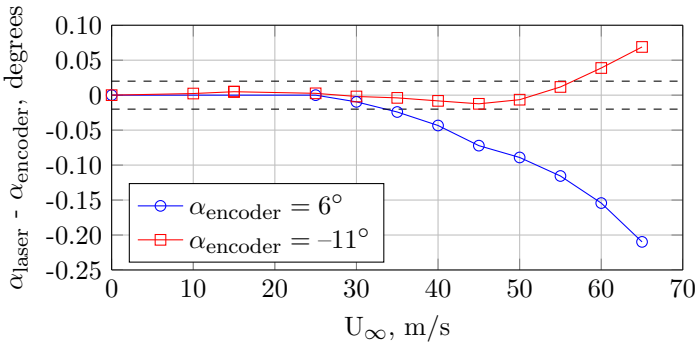

Figure 10: Model deflection at constant $\alpha_{encoder}$. Dashed lines represent the static measurement uncertainty of the laser system.

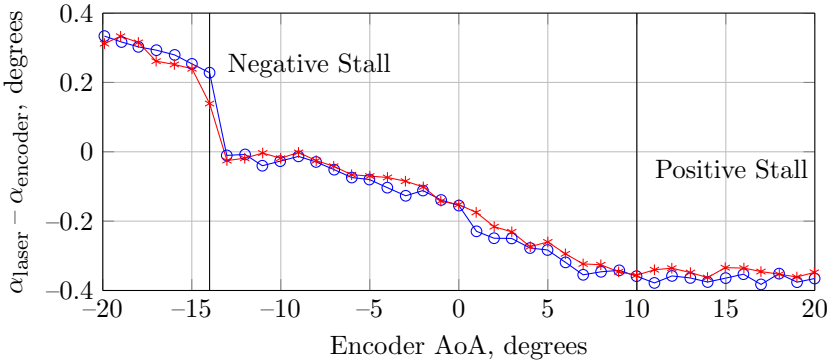

Figure 11: Difference between encoder angle of attack and laser angle of attack at $Re_c = 3.0$ Million for two consecutive runs.

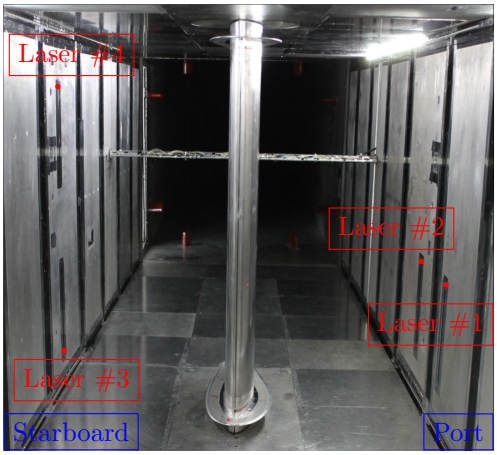

Figure 12: Laser distance sensor locations, looking downstream towards the model.

for an angle of attack sweep at $Re_c = 3.0$ Million. For this analysis, the center of rotation was assumed to not move during the test. Lasers 2-4 are 14-15" downstream of the center of rotation, while laser #1 is 6" upstream of the center of rotation. The discrepancy between laser #1 and lasers 2-4 shows that the DU96 is not simply rotating, but deforming in a more complex way.

Lasers 1 & 2, which are located at the same span location, were used to isolate model rotation and translation using measurements for both flow-on and flow-off conditions. Figure 14 shows the concept behind this calculation. With the flow off, the model was rotated through a set number of angles of attack. At each angle, the distances from both lasers were recorded. The flow was then turned on, and laser measurements were made at the same encoder angles of attack as the flow-off measurements. The laser distances from the flow-on and flow-off measurements were then used to calculate the rotation and wall-normal movement of the center of rotation.

Figure 15 shows the results from these calculations. The noise in the measurements is created by the uncertainty of moving the model to the exact same encoder angle of attack for flow-off and flow-on measurements. At this span location, the model is either bending or translating up to 1.5 mm in the direction of the applied lift (toward the starboard wall at negative angles and towards the port wall at positive angles.) In addition, the model is rotating between -0.25 and 0.20 degrees throughout the polar. The angle estimates from lasers 2-4, which were calculated assuming that the center of rotation is fixed, match the calculated rotation angle to within $\pm 0.1^\circ$. Lasers 2-4 are less sensitive to movement in the center of rotation and more sensitive to rotation because they are farther away from the center of rotation than laser #1. Moving forward, lasers 2-4 are used as the best measure of model angle of attack during flow-on measurements.

To further diagnose model deflections, the wind tunnel is constructing a structural loading rig. The rig is a steel structure that secures models using mounting hardware that closely matches what is used in the Stability Wind Tunnel. Three hydraulic pistons push against a loading bar, which applies a spanwise uniform load to the model at a desired chord location to simulate aerodynamic loading. Once a model is loaded, laser distance sensors are traversed along the span to measure deflection of the model. The loading rig will enable full measurement of model deflections across the entire span, which will further identify how the models are deforming (translating, bending, and rotating) under load.

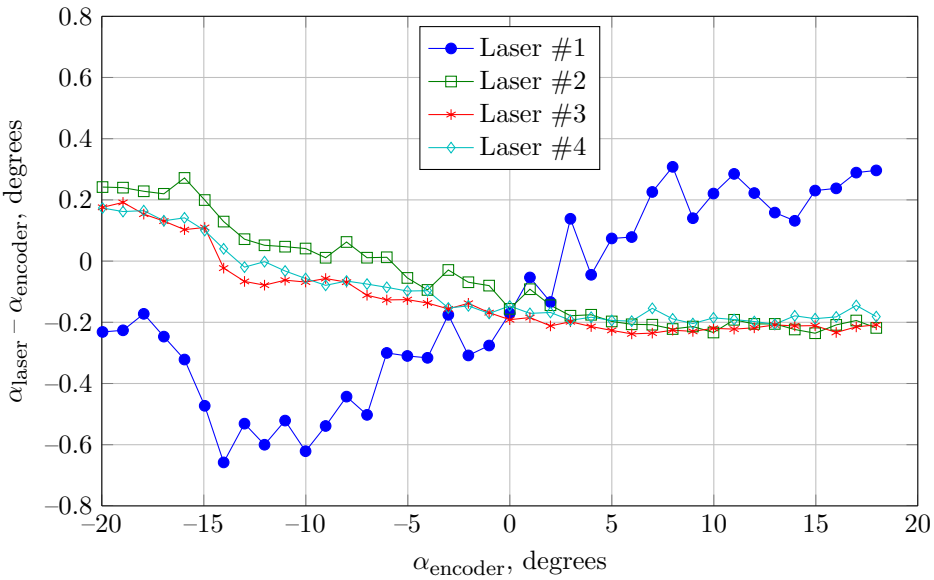

Figure 13: Rotation of the DU96-W-180 model at $\text{Re}_c = 3.0$ Million. Rotations calculated assuming the center of rotation is fixed.

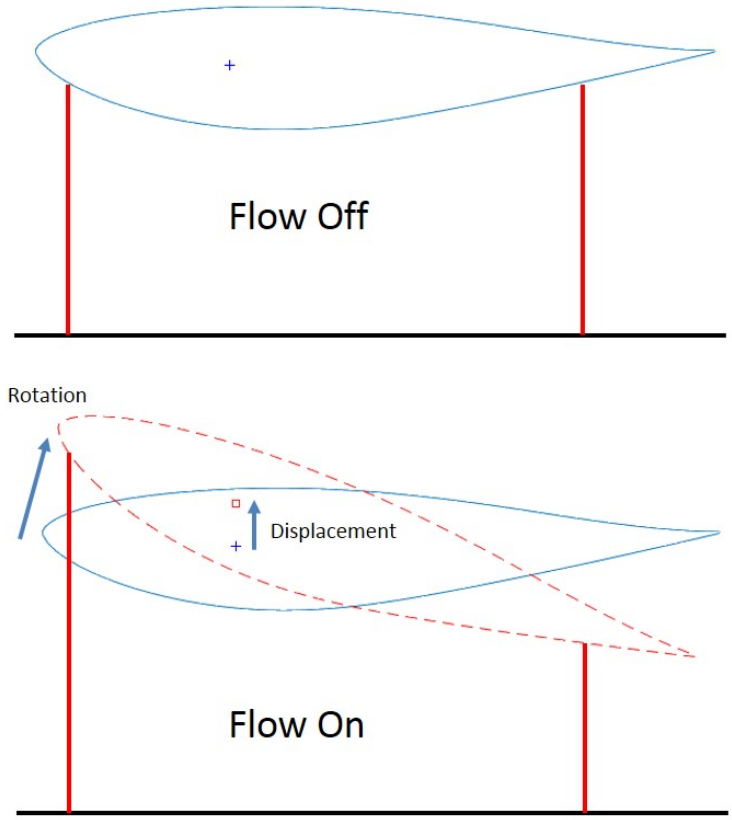

Figure 14: Displacement/rotation analysis using lasers 1 & 2.

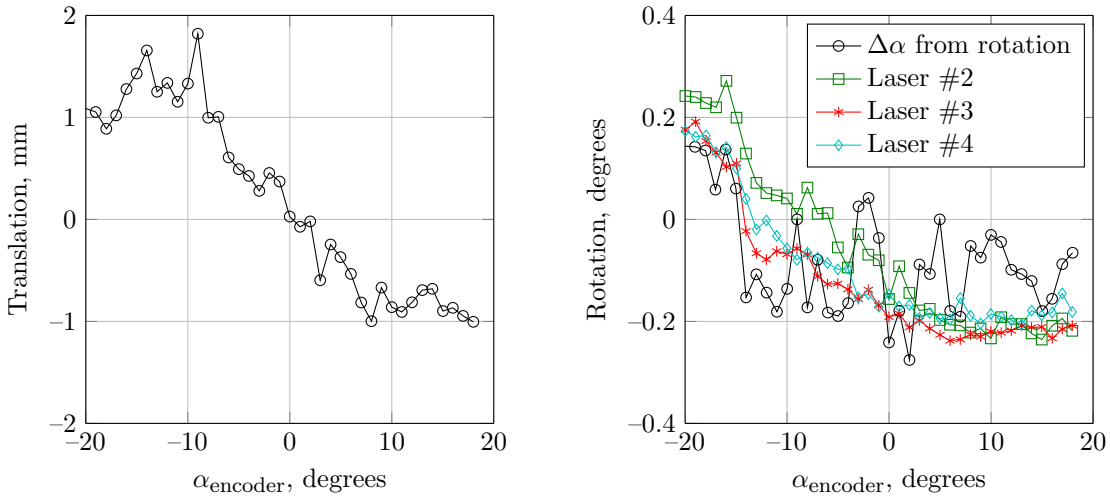

(a) Translation of the center of rotation towards the starboard wall.

(b) Model rotation, compared to measurements from lasers 2 through 4.

Figure 15: Translation and rotation of the DU96-W-180 (Re_c = 3.0 Million) at z/span = 0.37.

6 Summary & Ongoing Work

This paper described experiments in the Virginia Tech Stability Wind Tunnel to investigate all aspects of airfoil testing, from manufacturing through post-processing. These studies validated most aspects of testing and manufacturing used by the Stability Wind Tunnel but identified three areas for improvement.

Naphthalene sublimation tests showed model surface imperfections (burrs at the edges of laminates and 40 micron tape) creating turbulent wedges that prematurely led to boundary layer transition. The model surface quality of the DU96-W-180 model was improved by removing all tape from the surface and sanding/polishing surface defects. Improving the surface quality, and removing the associated turbulent wedges, increased the lift curve slope over 3%. These tests showed the importance of maintaining a high-quality model surface finish for clean airfoil measurements.

Pressure tap effects were investigated by installing additional pressure taps with varying geometries and diameters. Comparisons of clean and untripped cases showed a variation in the pressure measured by taps with varying diameters. This variation is consistent with the measurements of Shaw [5], who investigated similar effects in turbulent pipe flow. The effect is small, but not negligible, and is worst at high speed (up to $\Delta C_p = 0.02$ near the suction peak at Re_c = 3.0 Million.) Preliminary analysis suggests that using 1.0 mm ID pressure taps, instead of smaller taps, reduced the maximum measured lift coefficient by 0.004. This bias, as well as a turbulent wedge created by pressure taps at the leading edge, has driven the Stability Wind Tunnel to use 0.5 mm taps for all future models.

Finally, laser distance sensors were installed in the wind tunnel walls to measure model deflections under aerodynamic loads. The lasers yielded invaluable data regarding the bending/translation and rotation of the DU96-W-180 model during flow-on measurements. Lasers that strike the model near the trailing edge are most sensitive to model rotational deformation, and these lasers are used to measure an effective angle of attack to within $\pm 0.1°$. With the DU96-W-180 model, the rotations were significant enough to create a 1.6% difference in lift curve slope.

Ongoing work will further refine our understanding of model deflections and pressure tap diameter effects. The instrumented laminates on the DU96-W-180 model will be replaced with newly machined laminates with 0.5 mm pressure taps. Comparisons between measurements with the new taps and the original (1.0 mm) taps will highlight tap diameter effects. Finally, the structural loading rig will further diagnose how the DU96-W-180 model is deflecting under simulated aerodynamic loads and provide insights into how to modify model construction and/or model mounting to reduce the uncertainty caused by model deflections.

References

[1] WJ McCroskey. A critical assessment of wind tunnel results for the NACA 0012 airfoil. Technical report, DTIC Document, 1987.

[2] Niels Troldborg, Christian Bak, Helge Aagaard Madsen, and Witold Robert Skrzypinski. DAN-AERO MW: Final Report. Technical report, DTU Wind Energy, 2013.

[3] William J. Devenport, Ricardo A. Burdisso, Aurelien Borgoltz, Patricio A. Ravetta, Matthew F. Barone, Kenneth A. Brown, and Michael A. Morton. The kevlar-walled anechoic wind tunnel. *Journal of Sound and Vibration*, 332(17):3971 – 3991, 2013.

[4] Ken Brown, William Devenport, and Aurélien Borgoltz. Exploiting the characteristics of kevlar-wall wind tunnels for conventional aerodynamic measurements. AIAA Paper 2014-2110.

[5] R. Shaw. The influence of hole dimensions on static pressure measurements. *Journal of Fluid Mechanics*, 7:550–564, 4 1960.